EES Batteries

PAPER

View Article Online
View Journal | View Issue

Check for updates

Cite this: *EES Batteries*, 2025, **1**, 1762

Water-in-bisalt electrolyte for high-performance aqueous dual-ion battery

Dengyao Yang, [a] Huan Li,[a] Motonori Watanabe, [a] Miki Inada,[a,b] Aleksandar Staykov [a] and Tatsumi Ishihara *[a,b]

Received 27th June 2025,
Accepted 15th August 2025

DOI: 10.1039/d5eb00120j

rsc.li/EESBatteries

Aqueous dual-ion batteries (ADIBs) integrate safety, cost-efficiency, and power density to meet the demands of large electric storage in the future. However, the aqueous electrolyte still suffers from problems of small discharge capacity and low coulombic efficiency. In this work, a novel water-in-bisalt electrolyte (WiBS) was studied, and it was found that $LiN(SO_2F)_2$–$LiN(SO_3CF_3)$ (LiFSI–LiOTf) reaches an extremely high concentration of 39 mol kg^{-1} in water, and offers a wider electrochemical stability window of >3.1 V that is suitable for ADIBs. When applied as an electrolyte in DIBs, a high theoretical energy density of 264.05 Wh kg^{-1} is estimated, and a power density of 1440 W kg^{-1} and a discharge capacity of 94.3 mAh g^{-1} at 2 mA cm^{-2} are achieved in the initial cycle. Kinetics studies reveal that an LiFSI–LiOTf WiBS electrolyte exhibits a low activation energy for anion intercalation into a graphitic carbon cathode and also high diffusivity even at high concentration. Its high coulombic efficiency for charge and discharge can be explained by the prevention of the electrolysis of water by an extremely high concentration of electrolyte, such as 39 mol kg^{-1}. A stable cycle stability (>500 cycles) and also a high rate property are achieved in a cell using LiFSI–LiOTf aqueous electrolyte.

Broader context

It is demonstrated that increasing the concentration of support salt in water or water-based solvents leads to the formation of electrolytes with unique physicochemical properties, that can significantly enhance the performance of aqueous dual-ion batteries (ADIBs) in several key aspects. First, the electrochemical stability window of the aqueous electrolyte is significantly expanded by the high concentration of supporting salt, enabling the utilization of more electrochemically active electrode materials and broadening the operational voltage range of the battery. Second, the formation of solvated ion clusters and tailored ion pairing in high-concentration electrolytes enhances ion transport properties, resulting in faster charge–discharge kinetics and higher power density. This is particularly beneficial for ADIBs, which often suffer from higher ionic conductivity compared to their non-aqueous counterparts. Furthermore, the incorporation of dual salts in aqueous electrolytes offers additional advantages, such as the ability to independently tune the properties of cations and anions to optimize their compatibility with electrode materials while preventing side reactions. This, in turn, contributes to a substantial improvement in the cycle stability and overall lifespan of ADIBs.

Introduction

Dual-ion batteries (DIBs) are being developed that utilize an anion intercalation reaction in a graphite cathode at high potential, by which it is possible to obtain super high energy density compared to traditional rocking-chair batteries, and they have been attracting great interest.[1–3] However, traditional organic electrolytes show limited solubility of supporting salts, high viscosity, and low ionic conductivity, especially the diffusion rate of anions, which greatly restrict the electrochemical performance of dual-ion batteries.[4,5] As the active material of this battery is the supporting salt dissolved in the electrolyte, a high concentration of electrolyte is essentially required to provide high energy density for DIBs.[6,7] In addition, aqueous electrolytes that are intrinsically nonflammable and environmentally friendly would be ideal solutions.[8,9] However, the inherent limitations of aqueous electrolytes, such as the narrow window of electrochemical stability imposed by hydrogen and oxygen evolution, and high reactivity towards electrode materials, have confined the output voltage of such aqueous DIBs to below 1.8 V, resulting in severely compromised energy densities.[10–12] Therefore, expanding the electrochemical stability window of the aqueous electrolyte remains a significant challenge in developing aqueous DIBs with superior performance and high energy density.

Highly concentrated water-in-salt (WiS) electrolytes and hydrated electrolytes have emerged as promising strategies to

[a]*International Institute for Carbon-Neutral Energy Research (WPI-I2CNER), Kyushu University, Fukuoka, 819-0395, Japan. E-mail: ishihara@cstf.kyushu-u.ac.jp*
[b]*Department of Applied Chemistry, Faculty of engineering, Kyushu University, Fukuoka, 819-0395, Japan. E-mail: ishihara@cstf.kyushu-u.ac.jp*

Open Access Article. Published on 21 August 2025. Downloaded on 5/19/2026 3:37:02 PM. This article is licensed under a Creative Commons Attribution-NonCommercial 3.0 Unported Licence.

© 2025 The Author(s). Published by the Royal Society of Chemistry

Open Access Article. Published on 21 August 2025. Downloaded on 5/19/2026 3:37:02 PM. This article is licensed under a Creative Commons Attribution-NonCommercial 3.0 Unported Licence.

overcome the above challenges.[13–15] Suo *et al*. first introduced a novel class of WiS electrolyte containing 21 mol kg^{-1} lithium bis(trifluoromethanesulfonyl)imide (LiTFSI) dissolved in distilled water, which exhibited a remarkable electrochemical stability window of 3.0 V.[13] In such highly concentrated solutions, the $TFSI^-$ anion decomposes on the anode before water electrolysis, forming a dense, LiF-rich solid electrolyte interphase (SEI) layer on the anode. This protective layer effectively suppresses hydrogen evolution, thereby expanding the electrochemical stability window of the aqueous electrolyte.[16] Shortly thereafter, a hydrate melt electrolyte, $Li(TFSI)_{0.7}(BETI)_{0.3}{\cdot}2H_2O$, was reported, demonstrating a 2.7 V stability window on Pt electrodes, enabling the development of high-performance $LiCoO_2/Li_2Ti_2O_5$ batteries with energy densities exceeding 130 Wh kg^{-1}.[14] The wider electrochemical stability window (ESW) of these electrolytes is attributed to the significant reduction in free water clusters, which instead form crystalline hydrates coordinated with Li^+ ions in this highly concentrated aqueous system. Following these advances, extensive research has been conducted on the hydration and solvation structures of electrolytes, leading to a deeper understanding of their role in stabilizing aqueous battery systems.[17–19]

For dual-ion batteries, a wider ESW is even more critical than in aqueous lithium-ion batteries, as anion intercalation occurs at high potential (>4.5 V *vs.* Li) which is one of the attractive points of DIBs.[20,21] Research has shown that increasing the concentration of two or more salts beyond their solubility limits in aqueous media yield electrolytes with unique physicochemical properties, significantly enhancing the performance of aqueous dual-ion batteries (ADIBs).[22,23] First, the ESW of the aqueous electrolyte was significantly expanded by the high concentration of supporting salt, enabling the utilization of more electrochemically active electrode materials and broadening the operational voltage range of the battery.[24,25] Second, the formation of solvated ion clusters and tailored ion pairing in high-concentration dual-salt electrolytes enhances ion transport properties, resulting in faster charge–discharge kinetics and higher power density.[26,27] This is a particular benefit of ADIBs, which often suffer from higher ionic conductivity compared to their non-aqueous counterparts.[28] Furthermore, the incorporation of dual salts in aqueous electrolytes offers additional advantages, such as the ability to independently tune the properties of cations and anions to optimize their compatibility with electrode materials while preventing side reactions.[29,30] This, in turn, contributes to a substantial improvement in the cycle stability and overall lifespan of ADIBs.

It has been reported that aqueous electrolytes, particularly those approaching saturation, often exhibit high viscosity and low ionic conductivity.[31] Under such conditions, the cells experience reduced charge–discharge rates and diminished overall performance.[32,33] To date, aqueous electrolytes, especially pure aqueous electrolytes, have rarely be used in dual-ion batteries.[11,12,23] However, the use of a highly concentrated electrolyte is necessary in terms of the energy density of a dual-ion battery. In this study, we investigate the charge and discharge performance of a dual-ion battery using a novel water-in-bisalt (WiBS) electrolyte utilizing LiFSI and LiOTf, which have small kinetic diameters. 39 mol kg^{-1} LiFSI–LiOTf aqueous electrolyte exhibits an impressive electrochemical stability window of 3.1 V and a high O_2 evolution reaction potential. Raman and nuclear magnetic resonance (NMR) spectroscopy are employed, combined with density functional theory (DFT) calculations, to investigate how concentrated LiFSI and LiOTf stabilize water molecules across this expanded voltage range. Furthermore, this bisalt electrolyte was applied to develop an aqueous dual-ion battery (ADIB), with its electrical storage performance evaluated at both low and high charge rates. Based on the unique properties of these electrolytes, the limitations of conventional aqueous electrolytes are overcome, and the widespread adoption of ADIBs as a viable system is achieved.

Results and discussion

Electrochemical stability window

The wider ESM of WiS electrolytes resulted from the strong solvation interaction between water molecules, cations, and anions in the system. Therefore, the type of anion is an important parameter.[18,27] Fig. S1 shows LSV curves of several kinds of WiS and WiBS electrolytes that used familiar Li salts. The HER, OER onset potential, and ESW are summarized in Table S1. In this work, the onset standard of the HER and OER potential defined the potential at a current of 0.05 mA. For the single-salt electrolytes, the saturated concentrations of LiTFSI, LiFSI and LiOTf were 21, 30, and 21 mol kg^{-1}, respectively, and they showed ESW of 2.87 V, 3.16 V, and 2.80 V, respectively. Additionally, the LiFSI electrolyte exhibits an OER onset potential at 2.30 V, indicating that the Li^+ may interact strongly with water molecules, thereby more effectively suppressing water oxidation compared to $TFSI^-$ and OTf^- anions. In contrast, the LiOTf electrolyte presents the narrowest ESW, implying that OTf^- anions interact weakly with water molecules, which may facilitate a higher anion diffusion rate. Suo *et al*. further added LiOTf to 21 mol kg^{-1} LiTFSI WiS electrolyte to prepare 28 mol kg^{-1} 3LiTFSI–1LiOTf WiBS electrolyte and obtained a wider ESW due to a more compact and protective SEI being formed.[24,34] Li *et al*. relied on the high solubility of LiFSI and LiTFSI to yield 37 mol kg^{-1} 9LiFSI–1LiTFSI WiBS electrolyte, which delivered an ESW of 3.1 V, and a better OER onset potential, as displayed in Fig. S1.[23] According to Fig. S1, the OER onset potential is further shifted to a higher value upon the formation of the WiBS electrolyte, which can be attributed to enhanced ion–water interactions and structural compaction. Moreover, the elevated salt concentration in the WiBS electrolytes is advantageous for the development of high-energy-density DIBs.[4] LiFSI–LiOTf WiBS electrolytes were, therefore, prepared to develop high-energy-density and fast charging ADIBs, and the ratio was optimized from 5 : 5 to 9 : 1, as shown in Fig. 1. As the proportion of LiOTf decreased, the overall salt concentration increased, reaching 39 mol kg^{-1} at a compo-

© 2025 The Author(s). Published by the Royal Society of Chemistry

Open Access Article. Published on 21 August 2025. Downloaded on 5/19/2026 3:37:02 PM.
This article is licensed under a Creative Commons Attribution-NonCommercial 3.0 Unported Licence.

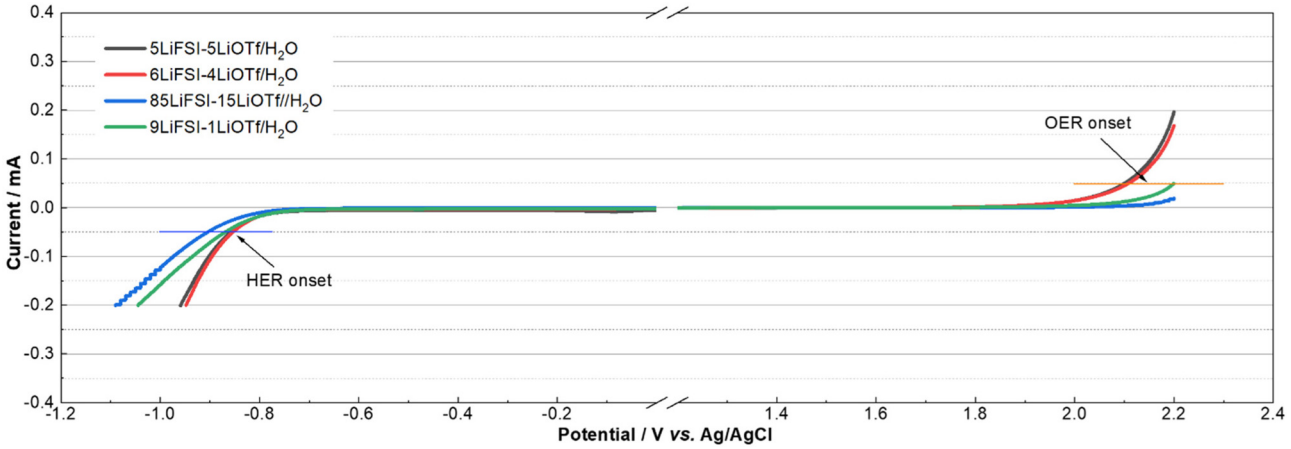

Fig. 1 Linear sweep voltammetry (LSV) of as-prepared aqueous LiFSI–LiOTf electrolytes on a Pt electrode within −1.1 to 2.2 V *vs.* Ag/AgCl at a sweep rate of 5 mV s^{-1}.

sition of 85 : 15 for LiFSI : LiOTf. When the proportion of LiFSI : LiOTf increased to 9 : 1, the saturated concentration decreased to 37 mol kg^{-1}, the same as that of the LiFSI–LiTFSI system. Fig. 1 shows the LSV curves of LiFSI–LiOTf WiBS electrolytes with varying ratios and concentrations. At a low LiFSI : LiOTf ratio, the lower salt concentration delivered a narrower ESW compared to higher concentration, and a lower amount of LiFSI in both WiBS electrolytes (5LiFSI–5LiOTf and 6LiFSI–4LiOTf) resulted in lower OER potentials of 2.10 and 2.11 V *vs.* Ag/AgCl, respectively. In contrast, the 85LiFSI–15LiOTf electrolyte showed HER and OER potentials of −0.91 V and >2.2 V, respectively, and the widest ESW of >3.1 V among all the electrolytes. Compared to a 37 mol kg^{-1} 9LiFSI–1LiTFSI electrolyte, as summarized in Table 1, the 85LiFSI–15LiOTf electrolyte showed better tolerance of water reduction, beneficial for obtaining high coulombic efficiency. The 9LiFSI–1LiOTf electrolyte shows a slightly narrower ESW to 85LiFSI–15LiOTf, indicating that high compaction could deliver a wider ESW.

The strong interaction of LiFSI–LiOTf WiBS electrolyte was further analyzed by first-principles density-functional-theory-based molecular dynamics (DFT-MD) simulation. Because of the strong interaction between water and Li salts, the density of the system increased, *i.e.*, the solvated ion pair cluster had a smaller free volume. The converted structure is shown in Fig. 2, and the analysis results of the model are summarized in Table 2. In the typical single-salt electrolyte, the end volume of the simulation result shows severe compression after 1 ps, and the end density of the solution states shows high compaction due to strong interaction as Li^+ interacts with six water molecules. With the building of a bisalt system, the end density of the electrolyte can be further compressed after conversion. For example, the end density of the LiFSI–LiTFSI system reached 1.72 g cm^{-3}, which was higher than that of the LiTFSI–LiOTf system, indicating stronger solvated ion pairs of Li with FSI^- and $TFSI^-$, which agreed well with our observation, as shown in Fig. 1. In the case of the LiFSI–LiOTf system, the end density was further increased to 1.76 g cm^{-3}, demonstrating that stronger interaction had been achieved, as the amount dissolved at saturation was 39 mol kg^{-1}. This strongly solvated ion cluster brings a wider ESW as electrolyte as displayed in Fig. 1. To reveal the actual compaction of WiBS electrolytes, the viscosity of the prepared electrolytes was tested and is shown in Fig. S2. Compared to LiTFSI–LiOTf, all LiFSI–LiOTf electrolytes show much lower viscosity, which demonstrates faster diffusion rates for cations and anions. Even when increased to 39 mol kg^{-1} for 85LiFSI–15LiOTf, it shows similar viscosity to 37 mol kg^{-1} 9LiFSI–1LiTFSI, indicating that the OTf^- anion shows weaker interaction and faster diffusivity compared to a single $TFSI^-$ anion.

Electrochemical performance of anion intercalation

Mo_6S_8 is a Chevrel-phase compound that enables substantial Li^+ intercalation, resulting in the delivery of high capacity.[35] Its intercalation potential is also well suited for application as an anode material in aqueous batteries; therefore, it was selected to assemble KS6/Mo_6S_8 ADIB as a full cell.[36] To elucidate the electrochemical interactions between the ions and electrodes, Fig. 3a and b display the CV curves of the Mo_6S_8 anode and

Table 1 Summary of information on HER and OER potential for aqueous LiFSI–1LiOTf electrolytes

Electrolytes	26 mol kg^{-1} 5LiFSI–5LiOTf	25 mol kg^{-1} 6LiFSI–4LiOTf	39 mol kg^{-1} 85LiFSI–15LiOTf	37 mol kg^{-1} 9LiFSI–1LiOTf	37 mol kg^{-1} 9LiFSI–1LiTFSI
HER potential/V *vs.* Ag/AgCl	−0.85	−0.85	−0.91	−0.89	−0.80
OER potential/V *vs.* Ag/AgCl	2.10	2.11	>2.20	2.19	2.30
ESW/V	2.95	2.96	>3.10	3.08	3.10

© 2025 The Author(s). Published by the Royal Society of Chemistry

Open Access Article. Published on 21 August 2025. Downloaded on 5/19/2026 3:37:02 PM.
This article is licensed under a Creative Commons Attribution-NonCommercial 3.0 Unported Licence.

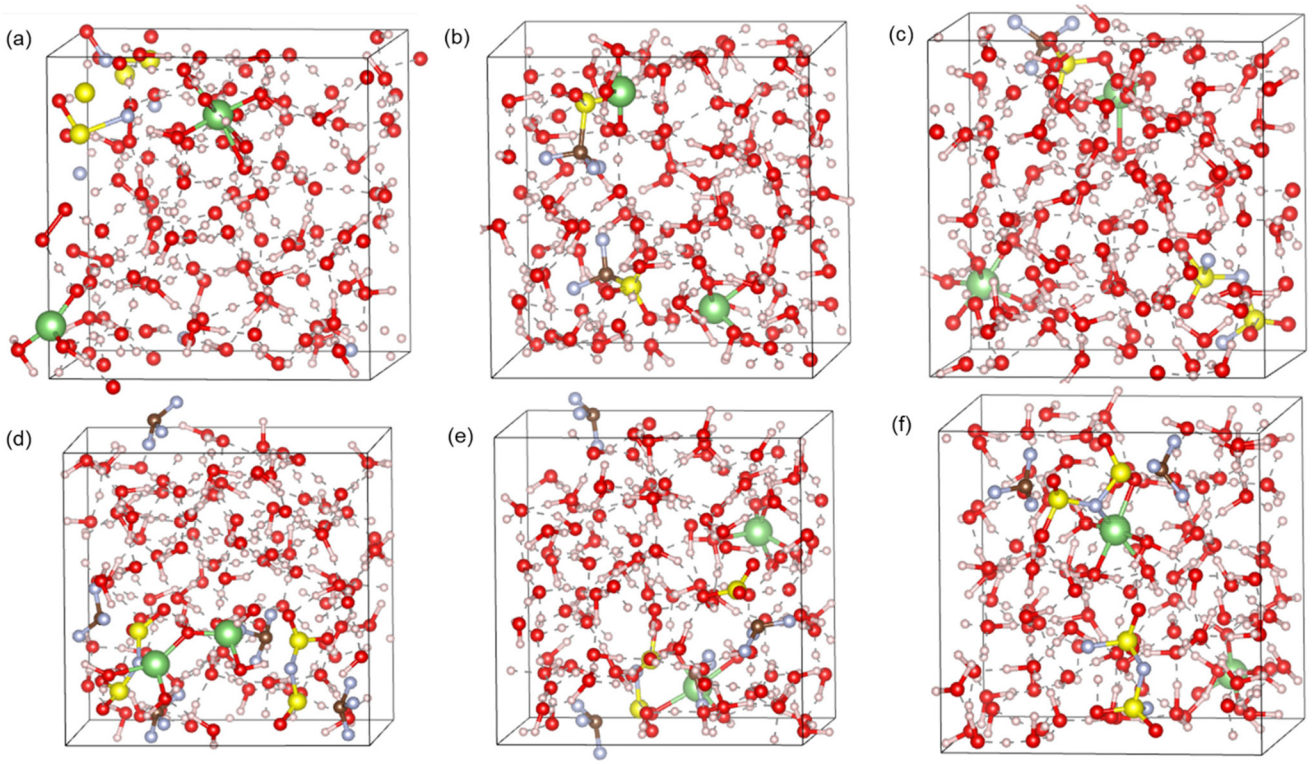

Fig. 2 Visualization of equilibrium trajectories obtained from first-principles DFT-MD simulations of 1-salt molecule/50-H_2O after 1 ps: (a) single LiTFSI, (b) single LiFSI, (c) LiOTf, (d) LiTFSi–LiOTf, (e) LiFSI–LiTFSI, (f) LiFSI–LiOTf. Atom colors: Li, green (presented at a larger size for emphasis); C, brown; H, white; O, red; S, yellow; F, blue. The cubic boxes represent the periodic boundaries of the supercells used in the DFT-MD simulations.

Table 2 Summary of DFT-MD simulation results after 1 ps for various component salts in water

Salts	LiTFSI	LiFSI	LiOTf	LiTFSI–LiOTf	LiFSI–LiTFSI	LiFSI–LIOTf
Starting volume	3944.95 Å^3	3612.79 Å^3	3509.63 Å^3	3727.29 Å^3	3778.87 Å^3	3651.21 Å^3
End volume	2335.73 Å^3	2249.75 Å^3	2132.12 Å^3	2282.38 Å^3	2201.74 Å^3	2070.85 Å^3
Starting density	1.00 g cm^{-3}	1.00 g cm^{-3}	1.00 g cm^{-3}	1.00 g cm^{-3}	1.00 g cm^{-3}	1.00 g cm^{-3}
End density	1.69 g cm^{-3}	1.60 g cm^{-3}	1.65 cm^{-3}	1.63 g cm^{-3}	1.72 g cm^{-3}	1.76 g cm^{-3}

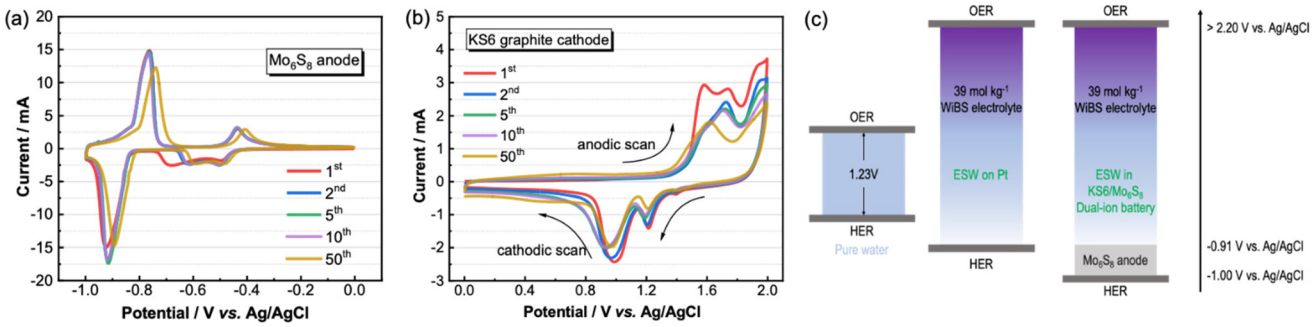

Fig. 3 Cyclic voltammetry (CV) profiles of (a) an Mo_6S_8/AC cell and (b) a KS6 graphite/AC cell using 39 mol kg^{-1} 85LiFSI–15LiOTf/H_2O electrolyte. (c) Illustration of extended ESW on Pt and in KS6/Mo_6S_8 dual-ion battery.

KS6 cathode, respectively, recorded in the 39 mol kg^{-1} 85LiFSI–15LiOTf WiBS electrolyte at a scan rate of 5 mV s^{-1} with an activated carbon (AC) counter electrode and an Ag/AgCl reference electrode. The CV measurement for the Mo_6S_8 anode was performed within the potential range of −1 to 0 V *vs.* Ag/AgCl. In the first cycle, three distinct reduction peaks

Open Access Article. Published on 21 August 2025. Downloaded on 5/19/2026 3:37:02 PM.
This article is licensed under a Creative Commons Attribution-NonCommercial 3.0 Unported Licence.

were observed, corresponding to Li^+ intercalation reactions. Notably, the peak at −0.7 V disappeared in subsequent cycles, which may be attributed to an irreversible phase transformation.[37] Additionally, two pairs of redox peaks exhibited a small potential separation, indicating low polarization during Li^+ intercalation/deintercalation processes in this high-concentration electrolyte. The cathodic scan curve exhibited no peak associated with water reduction on the Mo_6S_8 anode, enabling full and reversible utilization of its Li^+ storage sites. This result confirms that an Mo_6S_8 anode further expanded the ESW of the 85LiFSI–15LiOTf WiBS electrolyte due to its intrinsic stability against water reduction. After 50 cycles, the CV curves exhibited negligible changes, demonstrating the excellent stability of the 85LiFSI–15LiOTf WiBS electrolyte on the Mo_6S_8 anode. A CV test of the KS6 cathode was performed within the potential range of 0–2.0 V *vs.* Ag/AgCl, as shown in Fig. 3b. The current signals of anodic and cathodic scanning processes correspond to anion intercalation into and deintercalation from the KS6 cathode, respectively. During the anodic scanning, the current response began at approximately 1.4 V *vs.* Ag/AgCl, indicating the onset of anion intercalation. As the potential increased to 2.0 V, three distinct peaks were observed in the CV curve, corresponding to the formation of graphite intercalation compounds (GICs) at different stages.[38] During the cathodic scan, two peaks were observed at 1.0 V and 1.2 V *vs.* Ag/AgCl in the CV curves, assigned to the deintercalation of FSI^- anions, as confirmed in Fig. S3a. Additionally, a very weak peak appeared at approximately 1.4 V, which is attributed to the deintercalation of OTf^-, consistent with the data presented in Fig. S3b. It was, therefore, concluded that OTf^- also participated in the reactions of anion intercalation during anodic scanning. Fig. S3c and S3d present the CV curves of the KS6 cathode in 28 mol kg^{-1} 3LiTFSI–1LiOTf and 37 mol kg^{-1} 9LiFSI–1LiTFSI WiBS electrolytes. In comparison to the CV curves obtained using the 39 mol kg^{-1} 85LiFSI–15LiOTf WiBS electrolyte, these systems exhibited reduction peaks at lower potentials and larger redox potential differences. This suggests that the 85LiFSI–15LiOTf WiBS electrolyte may achieve higher energy density and improved rate performance. Furthermore, Fig. 3c compares the extended ESW of the WiBS electrolyte on a Pt electrode and within the KS6/Mo_6S_8 battery system, highlighting its remarkable stability on the Mo_6S_8 anode.

AC as an anode in ADIB shows low activity to hydrogen evolution,[39] full KS6/AC dual-ion batteries are, therefore, assembled to evaluate the viability of the LiFSI–LiOTf WiBS electrolyte at varying ratios and concentrations, as presented in Fig. 4a. Herein, the charge–discharge measurement adopted a capacity cut-off of 100 mAh g^{-1} due to the unknown optimal upper voltage for KS6/AC dual-ion batteries. Among them, the KS6/AC cell using the 85LiFSI–15LiOTf electrolyte exhibited the highest discharge capacity and best cycle stability upon 200 cycles, which can be attributed to the broader ESW provided. In contrast, the cells using the other three electrolytes exhibited lower capacities and rapidly lost stability over 50 cycles because of electrolyte decomposition. The cycle performance of the KS6/AC full cell using 30 mol kg^{-1} LiFSI and

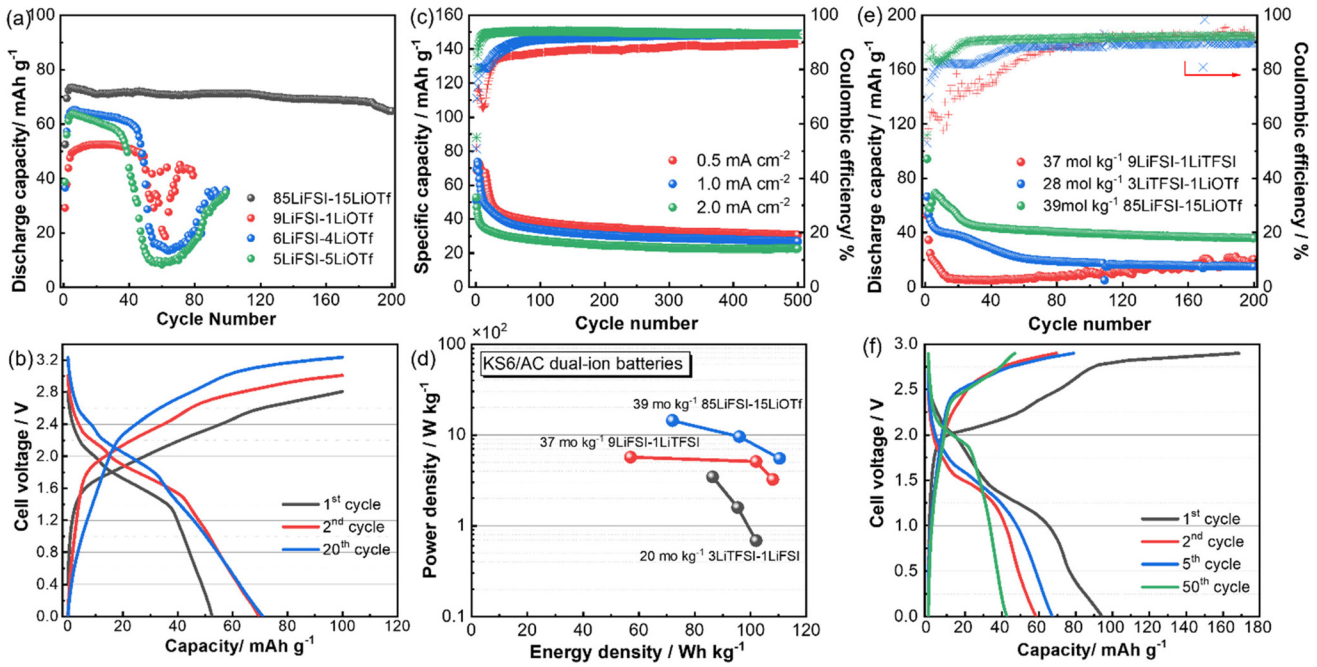

Fig. 4 (a) Cycle performance, and (b) charge–discharge curves of a KS6/AC battery using 39 mol kg^{-1} 85LiFSI–15LiOTf WiBS electrolyte with a capacity cut-off of 100 mAh g^{-1}. (c) Cycle performance of KS6/AC dual-ion batteries at varying current densities. (d) Ragone plot of previously reported KS6/AC dual-ion batteries and current work, (e) cycle performance and (f) charge–discharge curves of KS6/Mo_6S_8 dual-ion batteries within the voltage range of 0–2.9 V at 2 mA cm^{-2}.

© 2025 The Author(s). Published by the Royal Society of Chemistry

Open Access Article. Published on 21 August 2025. Downloaded on 5/19/2026 3:37:02 PM. This article is licensed under a Creative Commons Attribution-NonCommercial 3.0 Unported Licence.

21 mol kg^{-1} LiOTf WiS electrolytes is also shown in Fig. S4 for comparison. While using the saturated 30 mol kg^{-1} LiFSI WiS electrolyte, the KS6/AC cell showed a discharge capacity of around 30 mAh g^{-1} at the initial cycles and rapidly decreased to around zero, demonstrating poor stability (Fig. S4a). When 21 mol kg^{-1} LiOTf WiS electrolyte was used, the KS6/AC cell showed a discharge capacity lower than 30 mAh g^{-1} upon 100 cycles (Fig. S4b). It is evident that both the specific capacity and the cycling stability of the full cell were significantly enhanced by employing the 85LiFSI–15LiOTF WiBS electrolyte. As presented in Fig. 4b, a discharge capacity of 52.5 mAh g^{-1} was achieved at the initial cycle. Afterwards, the discharge capacity increased to 69.5 and 71 mAh g^{-1} for the 2nd and 20th cycles, respectively. A series of electrochemical performances of ADIBs in previously reported work is summarized in Table S2. Compared to those state-of-the-art ADIBs, this work presented high capacity, good rate performance, and high retention of capacity. Fig. S5 presents the electrochemical performance of KS6/AC cells upon upper voltages of 2.8 V (Fig. S5a and b), 2.9 V (Fig. S5c and d), and 3.05 V (Fig. S5e and f) to optimize the voltage range. With voltages of 2.8 V and 2.9 V, the cells showed high stability and reversibility over 500 cycles, but the cell showed a larger discharge capacity on cut-off at 2.9 V than that at 2.8 V (Fig. S5a and c). With a further increase in the upper voltage to 3.05 V, the cell delivered a higher discharge capacity but showed worse reversibility and stability, indicating that 3.05 V is too high and it causes electrolyte decomposition (Fig. S5e and f).

Fig. 4c shows the cycle performance of a KS6/AC cell using 39 mol kg^{-1} 85LiFSI–15LiOTf WiBS electrolyte at current densities of 0.5, 1.0, and 2.0 mA cm^{-2}. Clearly, the discharge capacity of the KS6/AC cell using 39 mol kg^{-1} 85LiFSI–15LiOTf WiBS electrolyte was slightly decreased, as the current density increased from 0.5 to 1.0 and 2.0 mA cm^{-2}, demonstrating good rate performance. Fig. S6 shows capacities of 68.72, 69.51, and 46.9 mAh g^{-1} in discharge curves of KS6/AC dual-ion batteries at corresponding current densities. After further cycling, the capacity decreased to around 40 mAh g^{-1} and retained a fixed value upon 500 cycles at 0.5 mA cm^{-2}. At a high current density of 2 mA cm^{-2}, the capacity shows a stable value of 30 mAh g^{-1}. Fig. S7a depicts XRD patterns of the KS6 cathode after charging and discharging in the KS6/AC battery using 39 mol kg^{-1} 85LiFSI–15LIOTf WiBS electrolyte. With charging to 3.0 V, the characteristic peak at 26.5° was split into 2 peaks which appear at 23.72° and 31.4°, that correspond to anion intercalation into the graphite layer to enlarge the gallery height, as displayed in Fig. S7b. I_{GH} and D_p denote the gallery height of two intercalated graphene planes and the repeat distance of the unit cell, respectively. In Fig. S7c, the parameters of the KS6 cathode after charging are summarized. Accordingly, the stage index was calculated from the most intense $(00n + 1)$ and $(00n + 2)$ reflections to be 2. I_{GH} and D_p were estimated to 0.79 and 1.125 nm, demonstrating that intercalants will enlarge the gallery height of the graphite layer.

Fig. 4d shows a comparison of the Ragone plot of previously reported KS6/AC dual-ion batteries and the current work, that was estimated based on the initial discharge capacity for all work. Compared to KS6/AC dual-ion batteries using 37 mol kg^{-1} 9LiFSI–1LiTFSI and 20 mol kg^{-1} 3LiTFSI–1LiFSI electrolyte,[31,40] the current cell exhibited higher energy density and power density due to its good rate performance, reaching 1440 W kg^{-1} at a current density of 2 mA cm^{-2}. To further investigate the good fast charging performance for 39 mol kg^{-1} 85LiFSI–15LiOTF WiBS electrolyte, KS6/Mo_6S_8 dual-ion batteries were assembled using different WiBS electrolytes to conduct charge–discharge measurement. The cycle performances of KS6/Mo_6S_8 dual-ion batteries using the corresponding WiBS electrolytes are depicted in Fig. 4e. At a current density of 2 mA cm^{-2}, the cell using 39 mol kg^{-1} 85LiFSI–15LiOTF shows higher capacity, and the other two electrolytes delivered a low capacity of 20 mAh g^{-1} upon 200 cycles. Additionally, better coulombic efficiency is also observed on the cell using 39 mol kg^{-1} 85LiFSI–15LiOTf that results from the wider ESW. Fig. 4f depicts the charge–discharge curves of a KS8/Mo_6S_8 dual-ion battery using 37 mol kg^{-1} 9LiFSI–1LiTFSI WiBS electrolyte at a current density of 2 mA cm^{-2}. It shows an initial discharge capacity of 94.3 mAh g^{-1}, but capacity is significantly decreased in the initial 20 cycles, and around 40 mAh g^{-1} is stably sustained up to 200 cycles. To sum up, ADIBs using 39 mol kg^{-1} 85LiFSI–15LiOTf WiBS electrolyte showed good electric storage and excellent rate performance.

To articulate how our concentrated electrolyte addresses key electrical energy storage challenges, such as safety and performance at low temperature, other studies were also conducted. As shown in Fig. S8, flammability evaluation was conducted on 39 mol kg^{-1} 85LiFSI–15LiOTf/H_2O electrolyte. Compared with a concentrated organic electrolyte of 5 mol kg^{-1} 1LFSI–1LiTFSI/DMC, the separator soaked with the concentrated organic electrolyte ignited immediately upon exposure to a flame, demonstrating high flammability (Video S1, SI 2). In contrast, a separator impregnated with aqueous electrolyte exhibited significantly different behavior. Despite prolonged exposure to a flame, the aqueous-electrolyte-soaked separator did not ignite, indicating nonflammable properties (Video S2, SI 3). Another problem of an aqueous electrolyte is freezing at low temperature. Fig. S9 shows the cycle performance of a KS6/AC dual-ion battery using 39 mol kg^{-1} LiFSI–15LiOTf/H_2O electrolyte at 0 °C. The defrosting function of an incubator introduced periodic fluctuations in the long-term cycle data. Nevertheless, as shown in Fig. S9a, the cell exhibited excellent stability and high coulombic efficiency over 500 cycles. Compared to a cell operating at 25 °C, the discharge capacity at 0 °C was slightly decreased, stabilizing at approximately 25 mAh g^{-1}. Fig. S9b exhibits the charge–discharge curves of the KS6/AC dual-ion battery at 0 °C. Despite the lower capacity compared to operation at 25 °C, the charge–discharge curves reveal a small overpotential for the anion intercalation reaction, indicating reasonable anion diffusivity sustained even at 0 °C.

Solvation structure of electrolyte

To further understand the extended ESW, Raman, and NMR spectroscopies were employed to investigate the solvation

Open Access Article. Published on 21 August 2025. Downloaded on 5/19/2026 3:37:02 PM. This article is licensed under a Creative Commons Attribution-NonCommercial 3.0 Unported Licence.

structure of LiFSI–LiOTf WiBS electrolyte. Fig. S10 shows the Raman spectra within the wavenumber range 300–650 cm^{-1} for 85LiFSI–15LiOTf WiBS electrolyte at varying concentrations. Two characteristic peaks identified at around 350 cm^{-1} and 462 cm^{-1}, are assigned to the stretching vibration of $-SO_3$ in OTf^- and wagging vibration of S–F in FSI^-.[41,42] At all concentrations, two peaks were always observed that demonstrated that no decomposition occurs for FSI^- and OTf^-. Upon increasing the concentration, the intensity of ρ_{S-F} gradually declined because of the shielding effects at high concentrations. Within the region of 700–800 cm^{-1}, the stretching vibration of S–N–S in FSI^- and bending vibration of CF_3 in OTF^- are located at 742 cm^{-1} and 762 cm^{-1} on the spectrum of 1 mol kg^{-1} 85LiFSI–15LiOTf electrolyte in Fig. 5a.[42,43] As salt concentration increased, the Raman peaks showed a redshift that indicates that anion contact ion pairs (CIPs) and anion aggregates (AGGs) gradually formed in electrolytes (Fig. 5a).[44] This phenomenon is also observed in single LiFSI and LiOTf electrolytes, as displayed in Fig. S11a and S11b. When the concentration reached 39 mol kg^{-1}, the peaks of S–N–S and CF_3 shifted to 756 cm^{-1} and 771 cm^{-1}, demonstrating an extreme solvation interaction between anion and water molecules. Fig. S11c presents the Raman spectra of 21 mol kg^{-1} LiOTf, 30 mol kg^{-1}, and 39 mol kg^{-1} 85LiFSI–15LiOTf electrolytes within the 700–800 cm^{-1} region. The spectrum for the 39 mol kg^{-1} 85LiFSI–15LiOTf electrolyte shows the CF_3 peak at the same wavenumber as that in the 21 mol kg^{-1} LiOTf electrolyte, indicating that the 6 mol kg^{-1} OTf^- in the 39 mol kg^{-1} 85LiFSI–15LiOTf electrolyte interacts strongly with the other components. Fig. 5b shows the Raman spectra within the region of 2800–3800 cm^{-1} that demonstrates the stretching vibration of O–H in water. Clearly, the peaks of asymmetric and symmetric stretching vibration of O–H in water are observed at 3235 cm^{-1} and 3420 cm^{-1}, respectively.[45] As salts dissolved in water, the peaks weakened and disappeared as the salt concentration reached 39 mol kg^{-1}, resulting in the appearance of a new peak at 3540 cm^{-1} (Fig. 5b). As shown in Fig. S11d and S11e, an identical phenomenon was observed for the single-salt electrolytes due to the solvation of water molecules with Li^+, as reported previously.[46] Here the stretching vibration peaks of O–H totally disappeared, suggesting that the original environment was broken and a new structure was built under high concentration.[14] Fig. S11f shows a comparison of different saturated solutions for Raman spectra within the region of 3000–3800 cm^{-1}. Different salts and concentrations caused the same phenomenon, implying that this change is related only to Li^+ and water molecules but not to anions. Fig. 5c presents a conceptual illustration of the proposed solvation structure in the WiBS electrolyte, based on Raman spectroscopy results. In this structure, H_2O molecules closely interact with both anions and cations, resembling the coordination environment found in crystalline hydrates. This

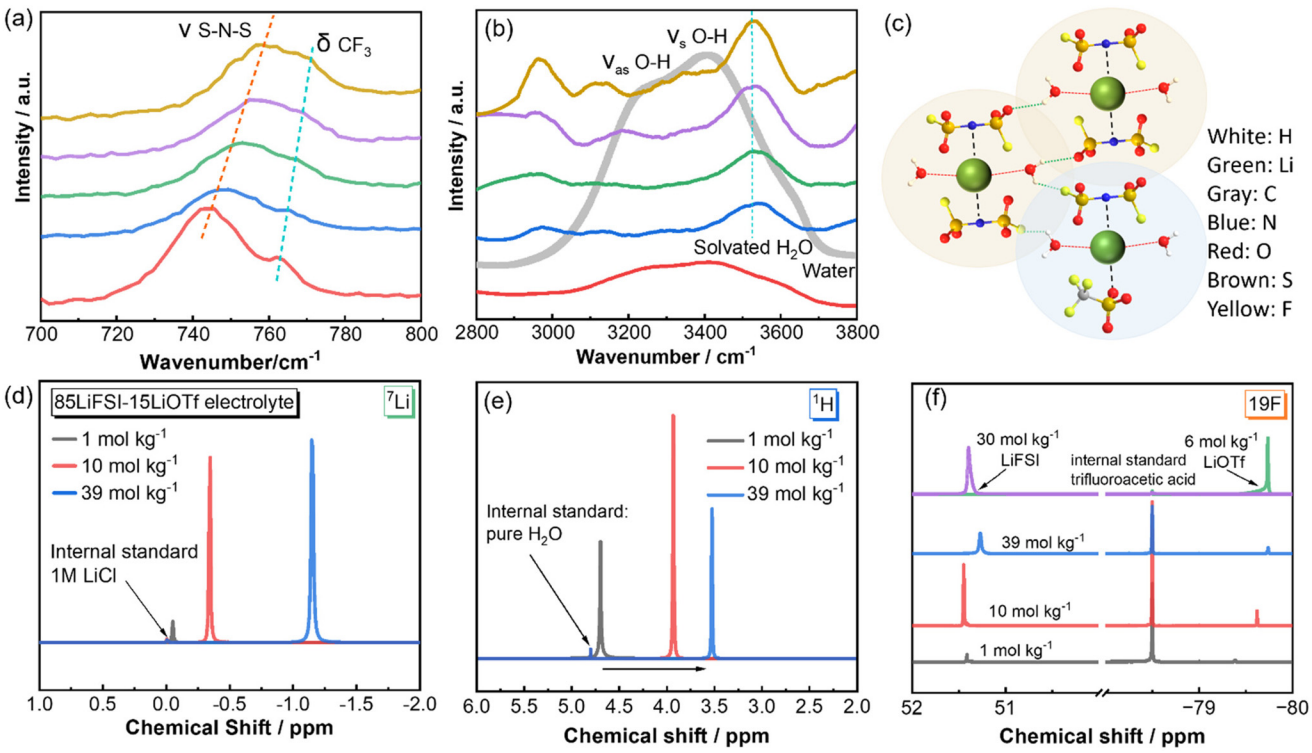

Fig. 5 Raman spectra of 85LiFSI–15LiOTF WiBS electrolytes at varying concentrations within (a) 700–800 cm^{-1} and (b) 2800–3800 cm^{-1}. (c) Illustration of the assumed network structure in WiBS electrolyte. (d) ^7Li, (e) ^1H and (f) ^{19}F NMR spectra of 85LiFSI–15LiOTf WiBS electrolytes at different concentrations.

© 2025 The Author(s). Published by the Royal Society of Chemistry

Open Access Article. Published on 21 August 2025. Downloaded on 5/19/2026 3:37:02 PM. This article is licensed under a Creative Commons Attribution-NonCommercial 3.0 Unported Licence.

unique solvation structure contributes to the extended ESW of the WiBS electrolyte.

NMR spectra were also acquired to understand the interactions between ions and water molecules for WiBS electrolyte, as shown in Fig. 5d–f. Fig. 5d shows the ^{7}Li chemical shift in 85LiFSI–15LiOTf solutions at varying concentrations, which was calibrated with 1 M LiCl solution. For 1 mol kg^{-1}, a single peak was identified at 0.05 ppm, that shifted slightly up-field, demonstrating that a larger anion increased the interaction between Li^+ and water molecules. As the concentration increased to 10 mol kg^{-1} and 39 mol kg^{-1}, the single peak progressively shifted further up-field to 0.35 ppm and 1.15 ppm, respectively, suggesting a uniform, singular environment for Li^+ ions and stronger interaction with water molecules. Fig. 5e shows the variation in the ^{1}H chemical shift with increasing concentration, calibrated against pure H_2O at 4.80 ppm. However, because of the remarkable increase in the amount of anions, the peak significantly shifted up-field at 3.8 ppm in 10 mol kg^{-1} solution and further shifted to 3.5 ppm in 39 mol kg^{-1} electrolyte, implying that water molecules may interact with anions by hydrogen bonds to form a new chain structure, as illustrated in Fig. 5c. The ^{19}F NMR chemical shifts were measured and are presented in Fig. S12 for the single-salt electrolytes and in Fig. 5f for the WiBS electrolytes. For the single-salt electrolytes, an up-field shift of the peaks with increasing concentration is observed in Fig. S12, with the peak regions corresponding to the F atoms in FSI^- and OTf^- identified in Fig. S12a and S12b, respectively. In Fig. 5f, an up-field shift is also observed with increasing concentration, consistent with the behaviour of the single-salt electrolytes. This suggests that anions interact with water molecules, forming a new network that replaces the hydrogen-bonding network of pure water, thereby suppressing the HER and OER in the WiBS electrolyte. Additionally, a noteworthy phenomenon observed in Fig. 5f is that the peak corresponding to the F atoms in OTf^- appeared in the same region for both the 6 mol kg^{-1} LiOTf electrolyte and the 39 mol kg^{-1} 85LiFSI–15LiOTf WiBS electrolyte, suggesting that the interaction strength involving OTf^- anions may be similar in both systems. In this situation, OTf^- might be state at a localized low interaction in 39 mol kg^{-1} WiBS electrolyte, that related to deliver a fast diffusion during charging.

Kinetics of anion intercalation

In a bid to uncover the underlying mechanisms behind the exceptional fast charging performance, CV and EIS were systematically employed to meticulously probe the kinetics of anion intercalation. CV measurement of the KS6 cathode was conducted in 39 mol kg^{-1} 85LiFSI–15LiOTf and 37 mol kg^{-1} 9LiFSI–1LiTFSI WiBS electrolyte at varying sweep rates of 2–10 mV s^{-1} within 0–2.0 V *vs.* Ag/AgCl, as depicted in Fig. 6a and Fig. S13a. In Fig. 6a, 5 peaks are marked P1–P5, and the peak maximum currents are summarized in Table S3. The

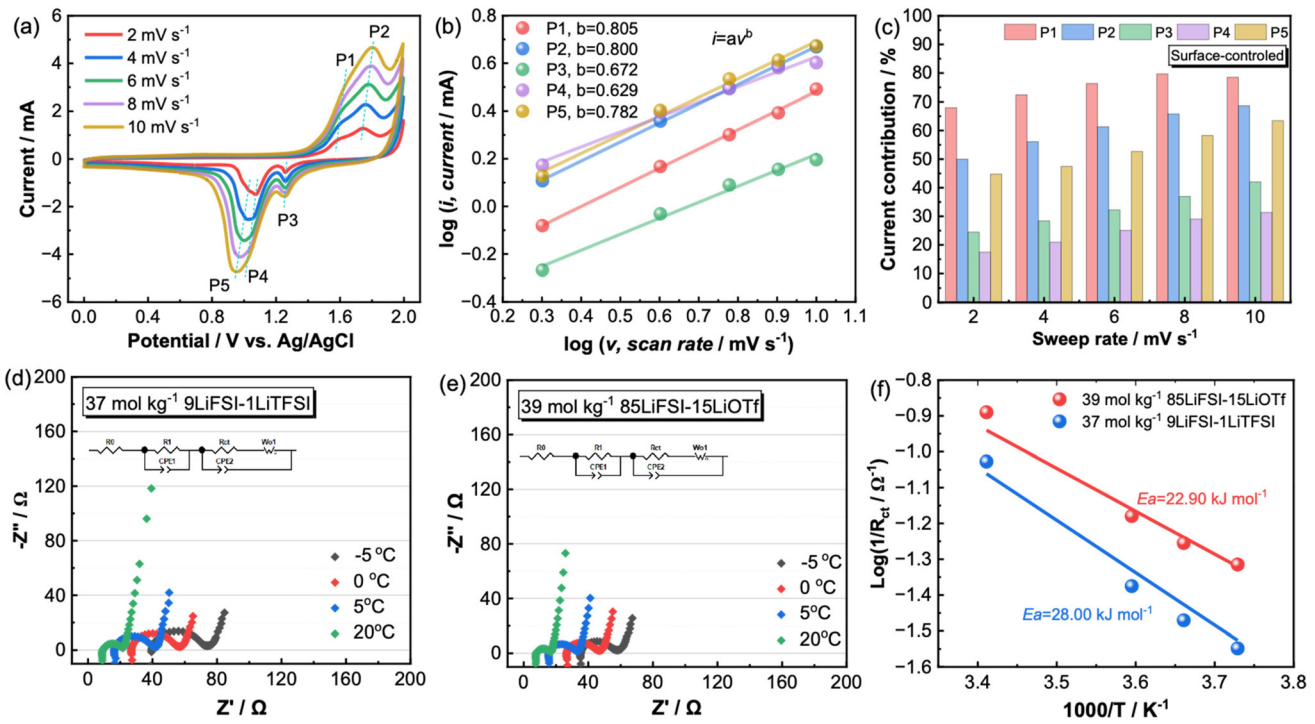

Fig. 6 (a) CV curves of KS6 cathode in 39 mol kg^{-1} WiBS electrolyte at varying scan rates. (b) Log *i versus* log *v* to determine *b* values for graphite cathodes with 39 mol kg^{-1} WiBS electrolyte. (c) The capacitive contribution towards anion storage at different sweep rates for a KS6 cathode in 39 mol kg^{-1} WiBS electrolyte at varying scan rates. Electrochemical impedance spectra (EIS) of the KS6 cathode in (d) 37 mol kg^{-1} 9LiFSI–1LiTFSI WiBS electrolyte and (e) 39 mol kg^{-1} 85LiFSI–15LiOTf WiBS electrolyte. (f) Arrhenius plots of log($1/R_{ct}$) *versus* 1000/*T* calculated from the EIS result and activation energy of anion intercalation.

© 2025 The Author(s). Published by the Royal Society of Chemistry

Open Access Article. Published on 21 August 2025. Downloaded on 5/19/2026 3:37:02 PM. This article is licensed under a Creative Commons Attribution-NonCommercial 3.0 Unported Licence.

relationship between peak maximum current (i) and sweep rate (v) follows the power law:[47,48]

$$I = av^b$$

where "a" and "b" are adjustable parameters, and the value of b determines whether the current comes from a surface-controlled contribution (b = 1) or a diffusion-controlled contribution (b = 0.5). As shown in Fig. 6b, the values of b could be estimated from the fitted line of $\log i$ *versus* $\log v$, and are 0.805, 0.800, 0.672, 0.629 and 0.782 for P1 to P5, respectively. The currents in the WiBS electrolyte are therefore considered to be the sum of both surface-controlled and diffusion-controlled contributions. The surface-controlled and diffusion-controlled contributions to the measured current could be quantified as follows:[47]

$$i = k_1 v^{1/2} + k_2 v$$

where $k_1 v^{1/2}$ and $k_2 v$ correspond to the diffusion-controlled contribution and surface-controlled contribution to the peak maximum current, respectively. Fig. 6c exhibits the surface-controlled contribution at various scan rates. It clearly shows that the current is dominated by the surface-controlled contribution during charging, and the percentage surface-controlled contribution is elevated as the scan rate increases. For the 37 mol kg^{-1} 9LiFSI–1LiTFSI WiBS electrolyte, the same estimation was carried out, as shown in Fig. S13b and S13c. In contrast, the percentage of surface-controlled contribution to current is much lower during charging, demonstrating that anion intercalation occurs more quickly in 39 mol kg^{-1} 85LiFSI–15LiOTf electrolyte.[49]

EIS was further executed at varying temperatures to explore the kinetics of the anion transfer process for the KS6 cathode, as shown in Fig. 6d and e for the KS6 cathode in 37 mol kg^{-1} 9LiFSI–1LiTFSI and 39 mol kg^{-1} 85LiFSI–15LiOTf electrolyte, respectively. The anion transfer resistances (R_{ct}) were estimated with the equivalent circuit in the inset (Fig. 6d and e) and are shown in Table S3. Here R_0, R_1 and R_{ct} are attributed to the resistance of the electrolyte, the contact resistance between the electrode particles and the metal current collector and charge transfer, respectively.[50,51] R_{ct} is the most important parameter relating to the kinetics of anion intercalation, which can be employed to estimate the activation energy of charge transfer as follows:[52,53]

$$\log\left(\frac{1}{R_{ct}}\right) = -\frac{E_a}{2.303RT} + A$$

were T is the Kelvin temperature, and R and A are the gas constant and Arrhenius constant, respectively. As shown in Fig. 6f, the activation energy of charge transfer was estimated from plots of the slope of $\log(1/R_{ct})$ against $1000/T$ s. After fitting and calculation, the E_a of anion transfer to the KS6 cathode in 37 mol kg^{-1} 9LiFSI–1LiTFSI and 39 mol kg^{-1} 85LiFSI–15LiOTf WiBS electrolytes are 28.0 and 22.9 kJ mol^{-1}, respectively. Additionally, Table S4 shows that the anion transfer resistance in 39 mol kg^{-1} 85LiFSI–15LiOTf electrolyte is smaller than that in 37 mol kg^{-1} 9LiFSI–1LiTFSI electrolyte, demonstrating that anions diffuse more easily in 39 mol kg^{-1} 85LiFSI–15LiOTf electrolyte. Therefore, it can be concluded that the anions in the structure of the 39 mol kg^{-1} 85LiFSI–15LiOTf WiBS electrolyte exhibit a greater tendency to intercalate into the KS6 cathode in ADIBs, owing to the high proportion of surface-controlled reactions and the rapid diffusion and transfer of anions.

Conclusions

Aqueous dual-ion batteries have attracted great attention owing to their intrinsically nonflammable and environmentally friendly nature, as well as their potential for high energy density in large-scale energy storage stations of the future. In this study, a novel WiBS electrolyte utilizing LiFSI and LiOTf was developed, which has smaller kinetic diameters compared to those reported previously. The WiBS electrolyte reached an extremely high concentration of 39 mol kg^{-1} in an aqueous system, which exhibited an impressive electrochemical stability window of 3.1 V from investigation of the LSV. Raman and NMR spectroscopy, combined with density functional theory calculations were employed to investigate how concentrated LiFSI and LiOTf stabilize water molecules across this expanded voltage range. This WiBS electrolyte was applied to develop an ADIB, and it delivered a good rate performance to KS6/AC dual-ion batteries, and the power density reached 1440 W kg^{-1} under a current density of 2 mA cm^{-2}. Additionally, this WiBS electrolyte also delivered better discharge capacity to a KS6/Mo_6S_8 dual-ion battery compared to 28 mol kg^{-1} 3LiTFSi–1LiOTf or 37 mol kg^{-1} 9LiFSI–1LiTFSI at a current density of 2 mA cm^{-2}. By harnessing the unique properties of these electrolytes, researchers can overcome the limitations of conventional aqueous electrolytes and pave the way for the widespread adoption of ADIBs as a viable and sustainable solution for future energy storage because of the expected high energy density of 264.05 Wh kg^{-1}.

Experimental

Chemicals

Lithium bis(fluorosulfonyl) imide ($LiN(SO_2F)_2$, LiFSI) and lithium trifluoromethanesulfonate ($LiN(SO_3CF_3)$, LiOTf) were purchased from Kishida Chemical. The active materials of the cathode (KS6, artificial graphite) and counter electrode (AC, activated carbon; 2090 m^2 g^{-1}) were purchased from Imerys Graphite & Carbon without further purification.

Preparation of materials

Mo_6S_8 preparation. MoS_2 (1 g, 6.263 mmol), CuS (0.398 g, 4.175 mmol), and Mo (0.602 g, 6.263 mmol) powders were used as raw materials. A mixture of the reactants (solvent/reactants = 2, by weight) was hand-ground and heated to 850 °C for 60 h and then cooled to room temperature. The product

© 2025 The Author(s). Published by the Royal Society of Chemistry

Open Access Article. Published on 21 August 2025. Downloaded on 5/19/2026 3:37:02 PM. This article is licensed under a Creative Commons Attribution-NonCommercial 3.0 Unported Licence.

was washed with hot deionized water and sonicated for 20 min to dissolve any remaining salt and to deagglomerate the particles. The products were stirred in a 6 M HCl solution for 12 h to extract Cu. Finally, the obtained powder (Chevrel Mo_6S_8) was washed with deionized water multiple times followed by drying at 100 °C overnight under vacuum.

Electrolyte preparation. The electrolyte solutions were prepared by dissolving LiFSI and LiOTf in distilled water. The 39 mol kg^{-1} LiFSI–LiOTf aqueous electrolyte was prepared by mixing LiFSI and LiOTf salts at a molar ratio of 85 : 15. For comparison, other WiBS electrolytes were prepared at molar ratios of 5 : 5, 6 : 4, and 9 : 1, respectively.

Electrochemical measurement

Linear sweep voltammetry (LSV) was carried out in a three-electrode cell by using Pt wire as working/counter electrodes, and an Ag/AgCl electrode as the reference electrode. Cyclic voltammetry (CV) measurements were performed using KS6 as the working electrode, an AC electrode as the counter electrode and Ag/AgCl as the reference electrode in a three-electrode cell. The KS6/AC half-cell was constructed in ambient atmosphere with a KS6 cathode, AC counter electrode, Ag/AgCl reference electrode, and a glass fiber separator; the loading mass for the KS6 cathode and Mo_6S_8 anode were *ca.* 1.0 and 1.5 mg cm^{-2}.

Characterization

Raman spectra were performed on a Raman spectrometer from HORIBA (HR 800) using a laser with a wavelength of 634 nm. Liquid NMR measurement was executed using a 400 MHz Bruker Avance NMR spectrometer (AV 400, Bruker), and the chemical shifts of ^1H and ^{19}F were calibrated with H_2O, and trifluoroacetic acid (TFA) for internal standards, respectively.

Computational detail

The liquid structure was theoretically studied on the basis of first-principles DFT-MD simulations based on the theory of the functional LDA PZ wavefunction NAO with QuantumATK software.[54,55] Molecular dynamics (MD) simulations were conducted with 100 water molecules and 2 salt molecules, starting at 1 g cm^{-3}. Different solution systems were simulated, denoted as the systems LiTFSI, LiFSI, LiOTf, LiTFSI–LiOTf, LiFSI–LiTFSI, and LiFSI–LiOTf. The equilibrium and production simulations were all performed in the NPT ensemble at constant pressure (1.00 bar) and temperature (300 K) in a cubic box with periodic boundary conditions in all xyz Cartesian directions. The simulation ran for 1 ps (1 fs per step). All the visualizations of MD simulations were implemented in the VESTA software package.

Conflicts of interest

There are no conflicts to declare.

Data availability

The data supporting this article have been included as part of the SI. See DOI: https://doi.org/10.1039/d5eb00120j.

Acknowledgements

This study was financially supported by the Grant-in-Aid for Scientific Research (A), No. 21H04700 from the Ministry of Education, Culture, Sports, Science, and Technology (MEXT) through Japan Society for the Promotion of Science (JSPS).

References

1 Z. Zhao and H. N. Alshareef, *Adv. Mater.*, 2024, **36**, 202309223.
2 W. Xu, L. Li, Y. Zhao, S. Li, H. Yang, H. Tong and Z. Wang, *Energy Environ. Sci.*, 2025, **18**, 2686–2719.
3 Y. Sui, C. Liu, R. C. Masse, Z. G. Neale, M. Atif, M. AlSalhi and G. Cao, *Energy Storage Mater.*, 2020, **25**, 1–32.
4 J. R. Dahn and J. A. Seel, *J. Electrochem. Soc.*, 2000, **147**, 899.
5 Y. He, Z. Chen and Y. Zhang, *iScience*, 2024, **27**, 110491.
6 H. Zhang, G. Guo, H. Adenusi, B. Qin, H. Li, S. Passerini and W. Huang, *Mater. Today*, 2022, **53**, 162–172.
7 S. Guan, Q. Peng, X. Guo, Y. Zheng, E. Liao, S. Sun, K. Shin, B. Liu, X. Zhou, C. Zou and Y. Tang, *Chem. Eng. J.*, 2024, **493**, 152864.
8 Z. Huang, Y. Hou, T. Wang, Y. Zhao, G. Liang, X. Li, Y. Guo, Q. Yang, Z. Chen, Q. Li, L. Ma, J. Fan and C. Zhi, *Nat. Commun.*, 2021, **12**, 3106.
9 X. Wu, Y. Xu, C. Zhang, D. P. Leonard, A. Markir, J. Lu and X. Ji, *J. Am. Chem. Soc.*, 2019, **141**, 6338–6344.
10 Y. Sui and X. Ji, *Chem. Rev.*, 2021, **121**, 6654–6695.
11 Y. Kondo, Y. Miyahara, T. Fukutsuka, K. Miyazaki and T. Abe, *Electrochem. Commun.*, 2019, **100**, 26–29.
12 H. Zhang, X. Liu, B. Qin and S. Passerini, *J. Power Sources*, 2020, **449**, 227594.
13 L. Suo, O. Borodin, T. Gao, M. Olguin, J. Ho, X. Fan, C. Luo, C. Wang and K. Xu, *Science*, 2015, **350**, 938–943.
14 Y. Yamada, K. Usui, K. Sodeyama, S. Ko, Y. Tateyama and A. Yamada, *Nat. Energy*, 2016, **1**, 16129.
15 J. Xie, D. Lin, H. Lei, S. Wu, J. Li, W. Mai, P. Wang, G. Hong and W. Zhang, *Adv. Mater.*, 2024, **36**, 2306508.
16 L. Suo, D. Oh, Y. Lin, Z. Zhuo, O. Borodin, T. Gao, F. Wang, A. Kushima, Z. Wang, H. C. Kim, Y. Qi, W. Yang, F. Pan, J. Li, K. Xu and C. Wang, *J. Am. Chem. Soc.*, 2017, **139**, 18670–18680.
17 S. Cai, X. Chu, C. Liu, H. Lai, H. Chen, Y. Jiang, F. Guo, Z. Xu, C. Wang and C. Gao, *Adv. Mater.*, 2021, **33**, 2007470.
18 D. Reber, R. Grissa, M. Becker, R. S. Kühnel and C. Battaglia, *Adv. Energy Mater.*, 2021, **11**, 2002913.
19 L. Chen, J. Zhang, Q. Li, J. Vatamanu, X. Ji, T. P. Pollard, C. Cui, S. Hou, J. Chen, C. Yang, L. Ma, M. S. Ding,

© 2025 The Author(s). Published by the Royal Society of Chemistry

Open Access Article. Published on 21 August 2025. Downloaded on 5/19/2026 3:37:02 PM. This article is licensed under a Creative Commons Attribution-NonCommercial 3.0 Unported Licence.

M. Garaga, S. Greenbaum, H. S. Lee, O. Borodin, K. Xu and C. Wang, *ACS Energy Lett.*, 2020, **5**, 968–974.
20 J. A. Seel and J. R. Dahn, *J. Electrochem. Soc.*, 2000, **147**, 899–901.
21 T. Placke, O. Fromm, S. F. Lux, P. Bieker, S. Rothermel, H.-W. Meyer, S. Passerini and M. Winter, *J. Electrochem. Soc.*, 2012, **159**, A1755–A1765.
22 C. Yang, J. Chen, X. Ji, T. P. Pollard, X. Lü, C. J. Sun, S. Hou, Q. Liu, C. Liu, T. Qing, Y. Wang, O. Borodin, Y. Ren, K. Xu and C. Wang, *Nature*, 2019, **569**, 245–250.
23 H. Li, T. Kurihara, D. Yang, M. Watanabe and T. Ishihara, *Energy Storage Mater.*, 2021, **38**, 454–461.
24 L. Suo, O. Borodin, Y. Wang, X. Rong, W. Sun, X. Fan, S. Xu, M. A. Schroeder, A. V. Cresce, F. Wang, C. Yang, Y. S. Hu, K. Xu and C. Wang, *Adv. Energy Mater.*, 2017, **7**, 1701189.
25 O. Borodin, J. Self, K. A. Persson, C. Wang and K. Xu, *Joule*, 2020, **4**, 69–100.
26 D. Yang, M. Watanabe and T. Ishihara, *Small Methods*, 2023, **7**, 2300249.
27 P. Jaumaux, X. Yang, B. Zhang, J. Safaei, X. Tang, D. Zhou, C. Wang and G. Wang, *Angew. Chem., Int. Ed.*, 2021, **60**, 2–11.
28 Y. Yamada, J. Wang, S. Ko, E. Watanabe and A. Yamada, *Nat. Energy*, 2019, **4**, 269–280.
29 K. Tasaki, A. Goldberg, J.-J. Lian, M. Walker, A. Timmons and S. J. Harris, *J. Electrochem. Soc.*, 2009, **156**, A1019.
30 D. Yang, J. Matsuda, J. T. Song, M. Watanabe and T. Ishihara, *J. Mater. Chem. A*, 2024, **12**, 13338–13347.
31 D. Yang, H. Li, M. Watanabe and T. Ishihara, *ChemSusChem*, 2023, **16**, e202201805.
32 J. M. Wrogemann, S. Künne, A. Heckmann, I. A. Rodríguez-Pérez, V. Siozios, B. Yan, J. Li, M. Winter, K. Beltrop and T. Placke, *Adv. Energy Mater.*, 2020, **10**, 1902709.
33 J. Zhu, Y. Xu, Y. Fu, D. Xiao, Y. Li, L. Liu, Y. Wang, Q. Zhang, J. Li and X. Yan, *Small*, 2020, **16**, 1905838.
34 L. Suo, O. Borodin, W. Sun, X. Fan, C. Yang, F. Wang, T. Gao, Z. Ma, M. Schroeder, A. von Cresce, S. M. Russell, M. Armand, A. Angell, K. Xu and C. Wang, *Angew. Chem., Int. Ed.*, 2016, **55**, 7136–7141.
35 L. Mei, J. Xu, Z. Wei, H. Liu, Y. Li, J. Ma and S. Dou, *Small*, 2017, **13**, 1701441.
36 L. Suo, F. Han, X. Fan, H. Liu, K. Xu and C. Wang, *J. Mater. Chem. A*, 2016, **4**, 6639–6644.
37 X. Zhu, J. Xu, Y. Luo, Q. Fu, G. Liang, L. Luo, Y. Chen, C. Lin and X. S. Zhao, *J. Mater. Chem. A*, 2019, **7**, 6522–6532.
38 M. Noel and R. Santhanam, *J. Power Sources*, 1997, **72**, 53–65.
39 J. W. Long, D. Bélanger, T. Brousse, W. Sugimoto, M. B. Sassin and O. Crosnier, *MRS Bull.*, 2011, **36**, 513–522.
40 D. Yang, M. Watanabe and A. Takagaki, *J. Electrochem. Soc.*, 2022, **169**, 120516.
41 M. Kerner, N. Plylahan, J. Scheers and P. Johansson, *RSC Adv.*, 2016, **6**, 23327–23334.
42 D. V. Radziuk and H. Möhwald, *Polymers*, 2011, **3**, 674–692.
43 T. D. Pham, A. Bin Faheem and K. K. Lee, *Small*, 2021, **17**, 2103375.
44 Y. Yamada, K. Furukawa, K. Sodeyama, K. Kikuchi, M. Yaegashi, Y. Tateyama and A. Yamada, *J. Am. Chem. Soc.*, 2014, **136**, 5039–5046.
45 Z. Hou, M. Dong, Y. Xiong, X. Zhang, Y. Zhu and Y. Qian, *Adv. Energy Mater.*, 2020, **10**, 1903665.
46 R. S. Kühnel, D. Reber and C. Battaglia, *ACS Energy Lett.*, 2017, **2**, 2005–2006.
47 T. Kim, W. Choi, H. C. Shin, J. Y. Choi, J. M. Kim, M. S. Park and W. S. Yoon, *J. Electrochem. Sci. Technol.*, 2020, **11**, 14–25.
48 X. Yang and A. L. Rogach, *Adv. Energy Mater.*, 2019, **9**, 1900747.
49 V. Augustyn, J. Come, M. A. Lowe, J. W. Kim, P. L. Taberna, S. H. Tolbert, H. D. Abruña, P. Simon and B. Dunn, *Nat. Mater.*, 2013, **12**, 518–522.
50 S. Lin, J. Xu and H. Li, *Energy Storage Sci. Technol.*, 2018, **7**, 732–749.
51 A. S. Keefe, S. Buteau, I. G. Hill and J. R. Dahn, *J. Electrochem. Soc.*, 2019, **166**, A3272–A3279.
52 W. Zhang, X. Sun, Y. Tang, H. Xia, Y. Zeng, L. Qiao, Z. Zhu, Z. Lv, Y. Zhang, X. Ge, S. Xi, Z. Wang, Y. Du and X. Chen, *J. Am. Chem. Soc.*, 2019, **141**, 14038–14042.
53 Y. Wang, Y. Zhang, S. Wang, S. Dong, C. Dang, W. Hu and D. Y. W. Yu, *Adv. Funct. Mater.*, 2021, **31**, 2102360.
54 A. J. Cohen, P. Mori-Sanchez and W. Yang, *Chem. Rev.*, 2012, **112**, 289–320.
55 G. Kinizia, *J. Chem. Theory Comput.*, 2013, **9**, 4834–4843.

© 2025 The Author(s). Published by the Royal Society of Chemistry